Contents lists available at ScienceDirect

Materials & Design

journal homepage: www.elsevier.com/locate/matdes

In situ micromechanical analysis of a nano-crystalline W-Cu composite

Michael Burtscher [a,*], Markus Alfreider [a], Christina Kainz [b], Klemens Schmuck [a], Daniel Kiener [a]

[a] *Department of Materials Science, Chair of Materials Physics, Montanuniversität Leoben, Jahnstraße 12, Leoben 8700, Austria*
[b] *Christian Doppler Laboratory for Advanced Coated Cutting Tools at the Department of Materials Science, Montanuniversität Leoben, Roseggerstraße 12, Leoben 8700, Austria*

HIGHLIGHTS

- Application of different complementary methods allowed insight into microstructural evolution as a function of applied deformation degree by HPT processing of a WCu alloy.
- Micro-mechanical properties such as *J*–Integral were determined by notched cantilever experiments.
- Sub nanometer precipitations were identified within nanometer-sized W grains using scanning transmission electron microscopy.
- Selection of optimal deformation state leads to a beneficial microstructure and tailored mechanical properties.

GRAPHICAL ABSTRACT
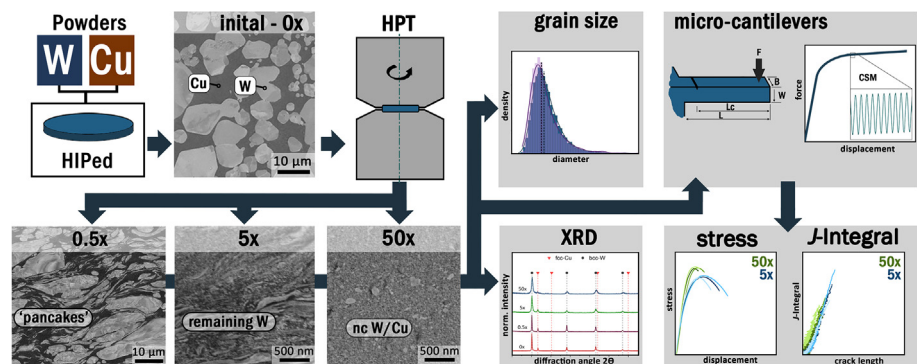
ABSTRACT

W-Cu composites are commonly used as heat-sinks or high-performance switches in power electronics. To enhance their mechanical properties and mutually their usability, grain refinement of the initially coarse-grained microstructure was realized using high–pressure torsion. This leads to different microstructural conditions, exhibiting fine-, ultrafine-grained or nanocrystalline microstructures. Scanning as well as transmission electron microscopy was performed to analyze the respective grain size and microstructures. The hardness and Young's modulus of the deformed specimens were quantified by nanoindentation testing. Furthermore, X-ray diffraction indicated a decreased grain size and changed lattice spacings upon increasing the deformation ratio. The deformed specimens were tested for their fracture behaviour by continuous stiffness measurements during in-situ microcantilever bending experiments. Here, mean *J*–integral values of 288 ± 38 J/m² and 402 ± 89 J/m² were determined for the 5 and 50 times turned specimens, respectively. The combination of different characterization methods applied on a W–Cu composite allows to identify both, beneficial and unfavourable microstructural components regarding the fracture properties.
© 2022 The Authors. Published by Elsevier Ltd. This is an open access article under the CC BY license (http://creativecommons.org/licenses/by/4.0/).

1. Introduction

Coarse-grained W-Cu materials are typically used as construction materials for high-current circuits in different media and are subjected to high local mechanical loads during switching

* Corresponding author.
E-mail address: michael.burtscher@unileoben.ac.at (M. Burtscher).

processes [1,2]. Furthermore, they are used as heat-sinks in power electronics and are therefore exposed to rapid temperature fluctuations [2-4].

These alternating loads cause fatigue cracks and later on failure of structural parts during overload events [5,6]. To counteract this, the material's damage tolerance must be increased by enhancing strength and ductility [7,8]. Typically, these material parameters are intrinsically mutually exclusive. However, this behaviour becomes less pronounced upon decreasing the grain size to the nanocrystalline (*nc*) regime [7,9]. Based on Hall-Petch hardening, the strength of the material is increased down to a typical grain size of about 10 nm. Below this dimension, strengthening is saturated due to enabled grain boundary sliding and other diffusional assisted processes [10]. Furthermore, the ductility can be increased by decreasing the grain size, enabling higher deformability and leading to more damage tolerant material behaviour [7,9-11]. This is typically valid in the ultra-fine grained regime but behaves differently in *nc* materials. Here, the fracture toughness (K_{IC}) is decreased due to a saturation level at a grain size of several nm [12-14].

The increasing demand for efficient power electronics and high–current switches exhibiting small component sizes with simultaneously long lifetime requires the development of materials capable to withstand higher loading under harsh conditions [2,15,16]. For that reason, strong efforts are made to develop new or enhance established material concepts [3,17-20].

Therefore, the current work aims to investigate the mechanical properties of a bulk W-Cu composite exhibiting different local grain size distributions. High-pressure torsion (HPT) deformed specimens were analyzed concerning their grain size and associated micromechanical properties [21,22]. To do so, the microstructure was determined by scanning electron (SEM) and transmission electron microscopy (TEM). This allows to identify critical microstructural components in both, the µm and nm–regime [22]. Furthermore, failure stress, *J*-integral and resulting fracture toughness were determined by in-situ micromechanical notched cantilever bending experiments. Young's modulus and hardness were quantified by nanoindentation experiments. The combination of the applied characterization methods allows to relate the micromechanical properties to the corresponding microstructures and to identify strengthening but also crack deflecting components. Furthermore, this type of experiment allows an in-situ investigation of the crack propagation on the relevant length scale.

2. Materials and methods

The W-33 wt% Cu composite was supplied as a rod material exhibiting a diameter of 8 mm from Plansee AG, Austria. The initial microstructure is displayed in Fig. 1a and consists of W and Cu grains. To refine the material, discs with a thickness of about 950 µm were cut from the rod and processed by HPT [23,24]. Therefore, the upper anvil was turned for 0.5, 5 and 50 rotations, resulting in an equivalent plastic strain of 5.7, 57.3 and 573% at a radius of 3 mm [22]. This was performed with an applied pressure of 7.4 GPa and a rotational speed of 1.2 rpm at room temperature (RT). The discs were cut and mechanically ground to lamellae with a thickness of 15–20 µm for micro–cantilever production. Additionally, polished quarters of the discs were used for imaging and nanoindentation experiments. In the following, specimens will be named according to the number of revolutions during the HPT process, e.g. 5 × in the case of the 5 times turned specimens. Generally, all experiments were conducted at a radius of 3.0 ± 0.2 mm to ensure comparable material conditions.

The microstructure was analysed with an SEM of type Leo 1525, Carl Zeiss AG, Germany, operating a field emission gun combined with the Gemini lens system. TEM images were recorded in scanning TEM (STEM) mode using a JEOL JEM-2200FS microscope from JEOL Ltd., Japan. SEM and STEM images were analyzed regarding their grain size using a Python 3.9 script including additional libraries as e.g. Scipy, Scikit-Image or OpenCV. The grain size was determined by an adapted watershed algorithm using the watershed class from the Scikit-Image library. To enable proper statistics, at least five different SEM or STEM images were analysed including more than 3000 individual grains.

The Young's modulus was measured for the 5 × and 50 × turned specimens by nanoindentation experiments utilizing a UMIS nanoindenter, Fisher–Cripps, USA, equipped with a diamond Berkovich tip, Synton MDP, Switzerland. To that, at least 20 indents were conducted for each specimen state within a load range of 10–20 mN, resulting in penetration depths between 210 and 330 nm. Data evaluation was performed according to the method of Oliver and Pharr [25]. The used Poisson's ratio of 0.35 for W-Cu was taken from ref. [26].

X-ray diffraction (XRD) measurements were performed on a Bruker-AXS D8 Advance, Bruker Corporation, USA, diffractometer in Bragg-Brentano geometry. Here, a 2θ range from 25 to 95° with a step size of 0.02°, a counting time of 0.5 s and Cu K$_\alpha$ radiation was utilized. The recorded diffractograms were evaluated using the Rietveld refinement method using the software package Topas 6, Bruker Corporation, USA [27].

In the following, bending beams were cut using a Zeiss Auriga Laser focused ion beam (FIB) system, by applying cutting currents from 1 to 5 nA. Final polishing and notching were performed with currents of 100 pA and 20 pA, respectively [28]. The attached FIB column was supplied by Orsay Physics, France including a Ga$^+$ ion source. Final dimensions of the produced and tested cantilevers concerning the height, width, length from the indenter tip to the notch and total length from the base to the indenter tip were determined to be about 3.5 ± 0.3 µm, 2.7 ± 0.3 µm, 11.5 ± 0.5 µm
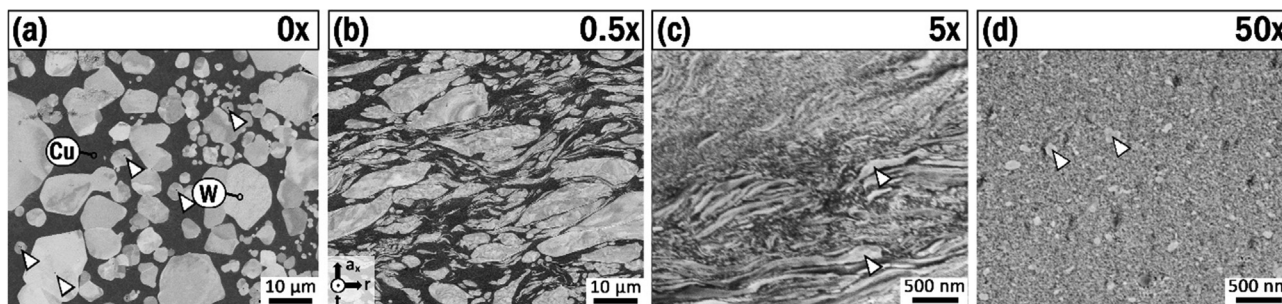

Fig. 1. SEM images of the microstructure of the investigated W-Cu specimen conditions at a radius of 3 mm. (a) The initial microstructure of the W-Cu rod, (b) 0.5 ×, (c) 5 × and (d) 50 × turned specimen conditions are displayed. White arrows in (a), (c) and (d) mark small pores located within W grains, remaining W platelets and globular W grains, respectively. In (b) a coordinate system is included, where the r, t and a$_x$ axis indicate the radial, transversal and axial directions, respectively.

and 13.0 ± 0.5 μm, respectively. The mean depth of the inserted notch was determined to be 924 ± 148 nm. However, in every case, the notch depth amounted to more than 30%, but not more than 40% of the height of the cantilever. In the case of the 0.5 × turned specimens, the notch was situated along or next to a W/Cu interface to determine the interfacial fracture behaviour. The respective TEM windows were cut directly next to the cantilevers at a diameter of about 3 mm from the center point of the HPT discs.

Micromechanical investigations were performed within an SEM LEO 1540XB, Carl Zeiss AG, Germany, using a Hysitron pico–indenter PI-85, Bruker Corporation, USA. The indenter is equipped with a continuous stiffness measurement (CSM) module, capable to record 300 data points per second. Data analysis was performed following the detailed description of Alfreider *et al.* [29] including a new analytical model to calculate the actual crack length from the current stiffness, Young's modulus and cantilever dimensions [30]. This allows determining the J–integral at any point of the in-situ experiment for every cantilever.

An estimation of the dimension of the plastic zone for coarse-grained W revealed a size of 31 μm [31,32]. In the case of Cu, this parameter varies in the mm range depending on deformation and microstructural conditions [33,34]. According to applied normative standards, the used cantilever dimensions do not fit the needed specifications [35,36]. In order to enable a comparison with literature data, fracture toughness (K_J) was determined from J–integral following ref. [35].

3. Results

Secondary electron (SE) SEM images of the initial microstructure of the W-Cu rod as well as the deformed counterparts are displayed in Fig. 1a-c. Due to a pronounced atomic contrast of the used SE detector, the bright phase constitutes W, the darker Cu grains. In Fig. 1a, equiaxed and globular W grains with a mean diameter of 4.21 ± 3.15 μm surrounded by a Cu matrix are visible. The high standard deviation of the analyzed W-grain size is reasoned by the used W powder. Occasionally, single pores can be identified in the received material situated within the W grains as exemplarily marked by white arrows. After 0.5 turns, a distinct elongation of the W grains can be determined from the SEM images (see Fig. 1b) [37]. Hence, a strong directionality of the mechanical properties is assumed next to the radial deformation degree [4]. The deformed W grains feature a ˙pancake˙ morphology, as they are elongated in radial (r) and transversal (t) but squeezed in the axial (a_x) direction. This leads to an anisotropic overlapping pancake structure, depicted in Fig. 1b [22,38]. Furthermore, the deformed microstructure no longer exhibits any pores within the W grains. The next deformation condition was reached by turning the anvils during the HPT process 5 turns. The respective microstructure is displayed in Fig. 1c and consists of equiaxed *nc* W grains within a Cu matrix next to areas with remaining elongated W grains. Based on SEM investigations, these areas exhibit a dimension of up to several μm in length and 1–2 μm in width with respect to the deformation direction of the HPT processed specimen. At a deformation of 50 turns, these persistent and elongated W grains have vanished as the deformation input was sufficient and a saturation level of the grain size could be reached [21]. As the microstructure exhibits a homogeneous grain size and no inhomogeneities, SEM images of this specimen are uniformly contrasted (see Fig. 1d).

To access the grain size of the 5 × and 50 × deformed specimens, TEM investigations were performed. STEM images including their normalized grain size distributions are displayed in Fig. 2. The μm sized W grains could not be analyzed within TEM, as they were not situated within the prepared TEM lamella. In the case of the 5 × turned specimen, a mean grain size of 6.7 ± 3.2 nm, as determined from 3516 individual grains, was obtained. The respective STEM image is displayed in Fig. 2a, where sub nm–sized particles could be identified within W grains (white arrows). In the corresponding grain size distribution (shown in Fig. 2b), they are not considered, as the minimum particle size was defined above their size. In Fig. 2c the microstructure of the 50 × turned specimen is displayed, exhibiting an average grain size of 7.0 ± 3.1 nm. Hence, a comparable grain size distribution could be determined for both specimen conditions in the homogeneous fine-grained areas. Also, in the case of the 50 × turned specimen, sub to nm–sized particles could be determined within W grains and are marked by white arrows. The corresponding distribution, including the diameters of both the W and Cu grains, exhibits an asymmetric behaviour, as the median ($\tilde{x}$), visible as a dashed vertical line in Fig. 2b and d, lies above the maximum values. The expectation values ($E[x]$) of the log-normal distributions were determined to be 5 nm and 6.3 nm in the case of the 5 × and 50 × turned specimens, respectively. As the $\tilde{x}$ and $E[x]$ are in good accordance and range within their estimated standard deviation, reaching the saturation level of the grain size is assumed in both cases.

XRD investigations were performed on all specimen conditions. In Fig. 3a, the X-ray diffractograms are displayed, including the standard peak positions of the body–centered cubic (bcc) W and face–centered cubic (fcc) Cu. The relative intensity of the Cu reflections decreases with increasing deformation ratio. A higher deformation degree is furthermore accompanied by a more pronounced peak broadening [21]. To obtain a quantitative measure of the peak broadening, the full width at half maximum (FWHM) as obtained from a Pseudo-Voigt fit of the 110-tungsten peak, is given in Fig. 3b. The step-wise increase of the FWHM with increasing deformation degree indicates a more pronounced micro–strain and a smaller size of coherently diffracting domains [27]. This result was substantiated by the SEM and TEM investigations, where a significant grain refinement of the 5 × and 50 × turned specimens could be determined (Fig. 1). Furthermore, the lattice parameters for Cu and W were calculated. However, only minimal changes from the theoretical values of W (3.165 Å) and Cu (3.615 Å) could be determined concerning the differently deformed conditions [21]. The phase fraction calculated by Rietveld analysis yielded a decrease in the Cu phase and an increase in the W phase fraction with increasing deformation degree [21,39,40]. This behaviour was also determined in the case of ball–milled W-Cu powders in ref. [40]. Generally, the W-Cu system is considered as an immiscible system at ambient pressure over the entire composition and temperature range [22,41]. However, during HPT or other severe plastic deformation processes, a distinct amount of Cu can be mechanically alloyed into the W phase and vice versa [21,22]. This may explain the decreasing amount of determined Cu phase fraction with increasing deformation degree.

Concerning the 5 × and 50 × turned specimens, valid nanoindentation experiments could be performed and a resulting Young's modulus of 204 ± 8 GPa and 208 ± 9 GPa, respectively, was determined. In addition, hardness measurements resulted in 8.0 ± 0.6 GPa in the case of the 5 × turned specimen, while the 50 × deformed specimen exhibited a hardness of 8.4 ± 0.7 GPa. The evaluated moduli and hardness values are in good accordance with literature data from a deformed *nc* W-Cu composite [42]. However, Young's modulus of the 0.5 × turned specimen was determined via the Reuss model for a composite material including a phase composition of 51/49 [43]. Hence, a calculated modulus of 188 ± 17 GPa was used for further evaluation [44,45]. Moduli data, determined via nanoindentation experiments, for this condition exhibits strong scattering due to the present grain size and directionality.
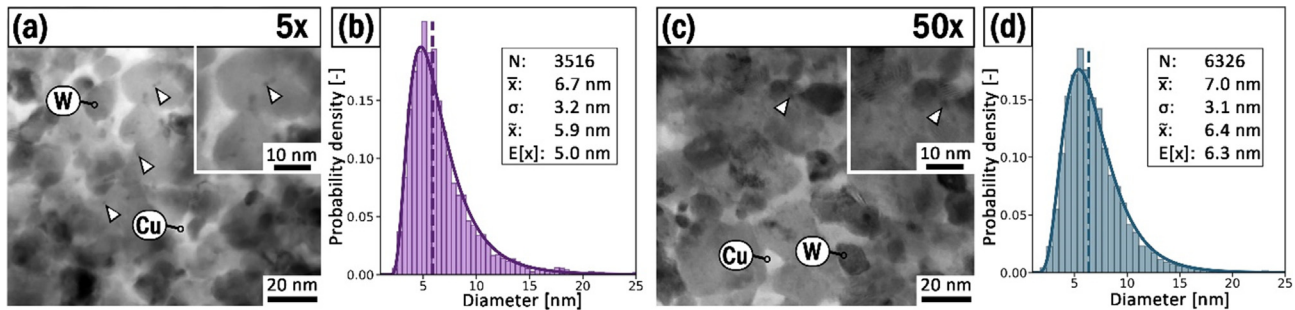
Fig. 2. Results from TEM investigations of the 5 × and 50 × turned specimens. In (a) and (c) STEM images of the nc microstructure of 5 × and 50 × turned specimens are displayed, respectively. Inserts in the right upper corner are displaying magnified areas including the sub nm–sized precipitations. Their corresponding log-normal distribution is visible in (b) and (d). Furthermore, sub nm–sized particles situated within W grains are marked by white arrows.
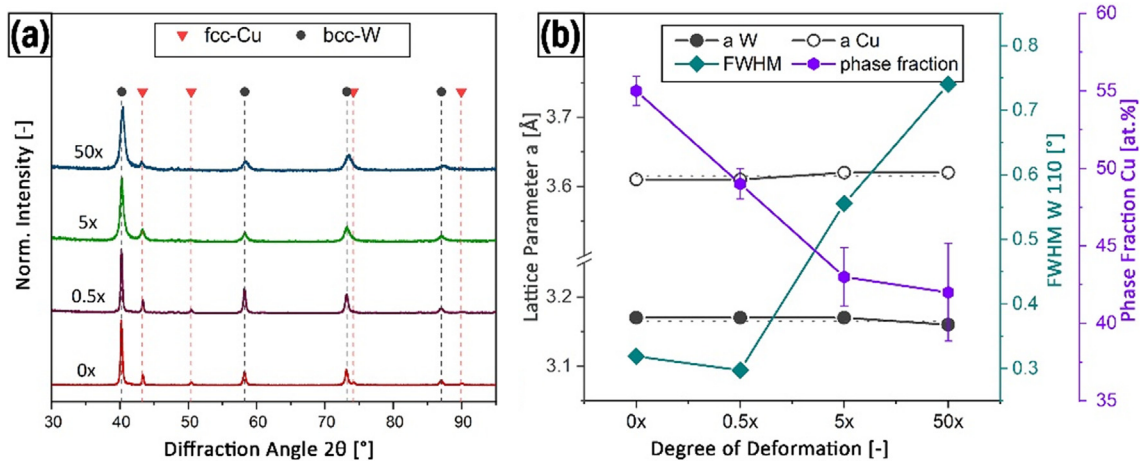

Fig. 3. (a) X-ray diffractograms from the undeformed (0 ×), 0.5×, 5 × and 50 × turned specimens. The theoretical peak positions of bcc–W and fcc–Cu are marked by vertical lines to guide the reader's eye. In (b), the respective lattice parameter of W and Cu, the FWHM of the 110 W peak and the phase fraction of Cu in at.% are displayed against the degree of deformation.

Determined maximum bending stress-displacement data for all deformed specimen conditions are displayed in Fig. 4a-c. Moderately deformed specimens exhibit a ductile deformation behaviour during the in-situ notched cantilever experiments. Depending on the location of the notch, varying fracture or blunting behaviour could be determined. However, during the experiments, no drastic drops in stress-displacement curves were determined until the fatal crack event or exceedance of the maximum displacement level. This indicates a stable crack growth until rupture of the remaining filament. In the case of 5 × or 50 × turned nc W-Cu specimens, a brittle to semi-brittle fracture behaviour was revealed. Nevertheless, the fine-grained microstructure enables higher fracture forces and therefore leads to higher resulting stress-displacement curves as displayed in Fig. 4b and c. The 50 × turned specimen tolerates higher displacement values and therefore higher bending strains until fracture of the cantilevers but overall lower fracture stresses were determined.

The calculated J-integral values plotted against the current crack length of all specimen types are displayed in Fig. 4d-f. The used actual crack length was calculated from the measured CSM signal during the in-situ experiments [29,30,35]. In the case of the 0.5 × turned specimens, the inhomogeneity of the microstructure due to the coarse grain size causes a noticeable variability of the J-integral (see Fig. 4a). Consequently, every single specimen is regarded separately, as the position of the notch and the presence of phases or interfaces along the crack path significantly influenced the experimental outcome. The calculated J–integral values

for the 5 × and 50 × turned specimens are shown in Fig. 4e and d, respectively. Furthermore, both specimen types indicate stable crack propagation for every single experiment without any sudden crack bursts or major crack events. Both specimen types exhibit only minor scattering of the resulting mechanical properties and show similar J–integral over crack length. This can be attributed to the more homogeneous microstructure of the 5 × and 50 × turned specimens as compared to the 0.5 × turned variant. However, the 50 × turned specimen exhibits higher plasticity and therefore, a distinctively higher J–integral and affiliated crack length could be reached.

To identify the effect of the actual microstructure on the crack propagation during the in-situ experiments, post-mortem SEM investigations of the fractured surfaces were performed. Selected images of the fractured surfaces, as well as their sketched microstructure in side–view, are displayed in Fig. 5. The sketches were reconstructed from the in-situ videos as well as pre- and post-mortem SEM investigations. The tested cantilever 0.5×_c1 was notched within a coarse W grain near a W/Cu interface (see a). However, during the in-situ test, a steady crack propagation through the massive W grain without any involvement of the near interface was determined. The SEM image reveals a smooth cracked surface along an unspecified W cleavage plane. As the crack front propagates through a randomly oriented W grain, the crack follows the easiest path and is therefore twisted from the ideal crack path. In the case of the 0.5×_c2 specimen, the crack propagated through a W grain, but was later stuck in the Cu phase
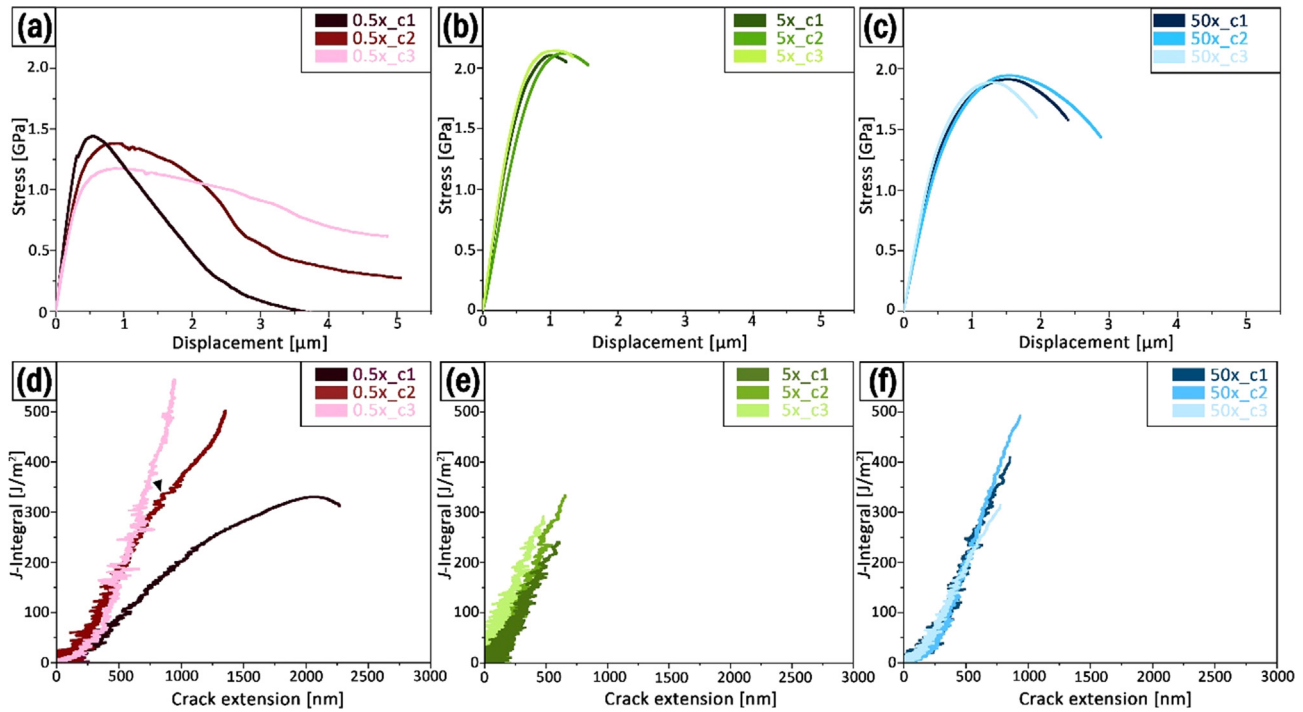
Fig. 4. Determined stress-displacement curves for (a) 0.5 ×, (b) 5 × and (c) 50 × turned W-Cu composite specimens. *J*-integral over crack length data from in-situ notched micro-cantilever experiments for (d) 0.5 ×, (e) 5 × and (f) 50 × turned W-Cu composite specimens. The black arrow in d) is pointing out an unstable crack burst of 110 nm of the 0.5×_c2 specimen. The crack length constitutes the current crack length from CSM subtracted by the specimen's notch depth.
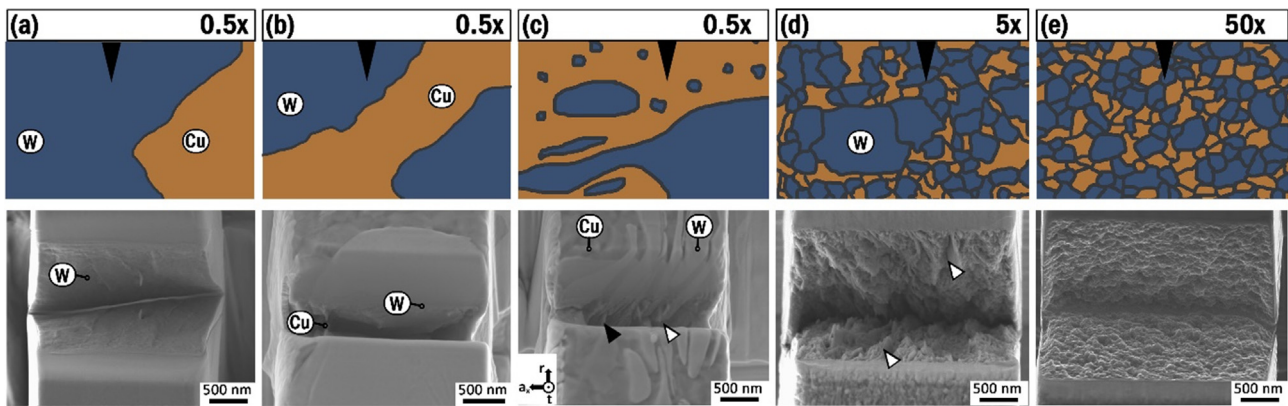

Fig. 5. Sketched side view of the microstructure (top) and their corresponding SE SEM images (bottom) of the fractured surfaces of selected cantilevers. In (a) specimen 0.5×_c1 containing a coarse W grain was notched near a Cu interface. Specimen 0.5×_c2 had a similar microstructure, but the crack was detained in the Cu phase (b). The sketch and SEM image in (c) display the microstructure of specimen 0.5×_c3, exhibiting a pancake structure. Here, black and white arrows indicate excerpted Cu and brittle fractured W along the fractured surface, respectively. Sections (d) and (e) depict the *nc* microstructure and fractured surfaces of 5 × and 50 × turned specimens, respectively. Black arrows in (d) indicate cleaved W grains along the fractured surfaces. In (c) a coordinate system was included, where r, t and a_x indicate radial, transversal and axial directions, respectively.

visible in Fig. 5b. Hence, the mechanical response determined from the in-situ experiments displayed in Fig. 4a and b are initially very similar.

Concerning the 0.5×_c3 specimen, the microstructure and fracture surface of a second cantilever from the 0.5 × turned specimen is displayed in Fig. 5c. Here, the notch was situated perpendicular to the pancake structure. Hence, the microstructure in front of the notch consists of alternating flattened W grains and the intermediate Cu phase. Upon analysis of the SEM images of the fractured surface, brittle fracture of the W grains (white arrow) with distinct fracture planes as well as ductile fracture of the intermediate Cu phase (black arrow) was determined [4]. Hence, the ductile Cu phase was elongated and ripped apart between the flattened W

grains visible in c. This combination leads to lower failure stresses, but the highest *J*–integral value within this study was achieved.

Both, 5 × and 50 × specimens exhibit a homogenous *nc* matrix as visible in Fig. 2. However, remaining coarse W grains are present within the microstructure of the 5 × turned specimen condition (Fig. 1d). The fractured surfaces reflect this circumstance by a rough surface appearance compared to the cleaved W grain in Fig. 5a. In the case of the 5 × turned specimen, a high number of undeformed W grains was determined via SEM analysis. Therefore, several cleaved W grains are visible on the fractured surface in Fig. 5d and two of them are marked by white arrows. As there is a distinct difference in mechanical properties determined via micromechanical cantilever experiments, this may be attributed

to the differences in the microstructure. Furthermore, the higher deformation of the 50 × turned specimen may cause an increased mechanical intermixing of the W and Cu phases and therefore, a different W/Cu interface structure (see e) [22,40].

4. Discussion

4.1. Microstructure

The microstructural evolution as a function of the applied deformation degree in the HPT process is visible in SEM images in Fig. 1a-d. With increasing deformation degree, the W grains are elongated in the deformation directions (see b) and further decreased in their size (c and d). The Cu grains represent the matrix phase and fill the interstices between the W grains. Detailed TEM investigations unveiled a mean grain size of the particles of 6.7 ± 3.2 and 7.0 ± 3.1 nm in the case of the 5 × and 50 × turned specimens, respectively. STEM images furthermore revealed sub nm–sized particles within the W grains, which are marked by white arrows in Fig. 2a and c. During the HPT process, significant pressure and temperature increment due to the deformation may lead to a higher solubility of Cu in W and vice versa. When finished, the specimen is released and cooled down to RT. As the driving force to dissolve dissimilar atoms consequently decreases, sub nm-sized Cu precipitates are formed within W grains [21,22,46,47]. However, no W particles were identified, as the temperature was too low to enable W diffusion in Cu grains [48]. Furthermore, there was no significant difference in size and number of the precipitates between the 5 × and 50 × turned specimens. Therefore, a similar amount of mechanically intermixed Cu is assumed to be soluble in the W grains for both specimen conditions. Precipitation of sub nm–sized particles within the W-Cu system was also achieved with additional alloying elements summarized by C. Hou et al. [20]. XRD measurements indicated a strong decrease of the grain size with a rising number of turns in the HPT process, as the peak broadening increased. Furthermore, a small peak shift indicates the change of the lattice parameters due to mechanical deformation and alloying [21]. However, the lattice parameters of the 5 × and 50 × turned specimens regarding the W and Cu phases are almost equal. Rietveld analysis indicated a pronounced reduction of the Cu phase fraction with increasing deformation degree [22,39]. In the case of the 5 × and 50 × turned specimens, a similar phase fraction was determined. Hence, the deformation during the HPT process was mainly dissimilated within the Cu phase as the W grain size stays similar for both, the 5 × and 50 × turned specimens. Here, the formation of Cu/Cu interfaces, dislocations and a pronounced deformation-induced intermixing especially along the W/Cu grain boundaries is assumed [40]. The combination of these mechanisms leads to an underestimation of the Cu phase fraction in the XRD determinations [22]. In the SEM images in Fig. 1c and d, numerous remaining W grains with a mean grain size of several hundred nm up to a few μm are visible. Their number decreases with increasing deformation ratio, as in the case of the 50 × turned specimen fewer remaining coarse W grains could be determined within the *nc* W-Cu composite microstructure. However, as the 5 × turned specimen nearly and the specimen 50 × turned specimen by far reached the saturation level, further deformation to higher numbers in turns would not lead to a significant decrease of prevalent coarse W grains.

4.2. Micromechanical fracture behaviour

The notch induced along the 0.5×_c1 specimen was situated within a coarse W grain, leading to stable crack growth during the in–situ experiment. Calculated from CSM data, a maximum J-integral of 330 J/m^2 at a crack length of 2038 nm was determined. From this, a maximum K_J value was calculated with 8.4 MPa$\sqrt{m}$, which is comparable to single crystalline W tested by microcantilever experiments within the same ligament range [49]. However, the notched W grain within the W-Cu cantilever exhibits no special orientation and therefore, the crack deviates marginally from the ideal notch direction (see Fig. 5a). Furthermore, post-mortem SEM investigations of the fractured surface of the cantilever unveiled a relatively smooth and cleaved crack surface. This indicates no influence of the Cu phase on the crack propagation, as a coarse W grain was tested and cleaved during the experiment.

In the case of the 0.5×_c2 cantilever, also a coarse W grain was notched near a W/Cu interface. During the experiment, the crack propagates through the W grain and is later trapped within the more ductile Cu phase [4]. The change from brittle fracture through the W grain to ductile behaviour, including plastic deformation and crack tip blunting within the Cu phase, is visible in Fig. 4a and the supplementary figure S1b. Consequently, the bending stress reaches a maximum of 1.38 GPa and decreases steadily to a displacement of 2.4 μm. Here, a sudden crack propagation of about 110 nm could be determined with a J–integral of 335.9 J/m^2 and is marked by a black arrow in Fig. 4d, which is equivalent to a fracture toughness of 8.5 MPa$\sqrt{m}$. This event is attributed to the failure of the remaining W ligament and subsequently the intercept of the crack tip to the Cu phase. The distinct difference in crack length to J–integral behaviour compared to the 0.5×_c1 specimen is attributed to the composite nature of the microstructure [50,51]. Thus, the crack is retarded within the ductile Cu phase. During further displacement, the adjacent force is decreased as the supporting cross-section is reduced and bending stresses are lowered. Furthermore, distinct crack tip blunting accompanied by minimal crack propagation within the Cu phase was determined [4,13,52].

The third specimen from the 0.5 × turned material contains a pancake structure visible in Fig. 1b between the coarse W grains and the remaining Cu matrix. The structure consists of elongated W platelets and an intermediate Cu matrix. These pancakes were cut perpendicular as the foil was prepared from one-quarter of the HPT disc. Therefore, several elongated W grains and Cu matrix in between are separated simultaneously. During testing and after initial approach, the J–integral against the crack length curve steadily increases. This indicates continuous crack propagation during loading, which was verified by SEM videos recorded during testing. Furthermore, no drastic drop in J-integral over crack length could be determined. In side–view, distinct crack tip blunting was determined as the ductile Cu allows high deformation prior to failure (see supplementary figure S1c) [12]. Thus, by further tuning this composite consisting of ductile Cu in combination with strengthening W platelets, an improved fracture tolerant microstructure may be achieved [20].

Regarding the 5 × turned specimens, a homogenous *nc* matrix exhibiting a mean grain size of 6.7 ± 3.2 nm was determined by TEM investigations. Complementary SEM investigations unveiled remaining W grains within the *nc* composite microstructure with a maximum size of several μm. The similar initial state of the bending beams leads to closely related stress over displacement and J-integral over crack length curves, visible in Fig. 4b and e, respectively. Hence, a mean J-integral of 288 ± 38 J/m^2 resulting in a mean calculated K_J of 8.2 ± 0.7 MPa$\sqrt{m}$ were determined from micro-mechanical tests before fatal fracture. Visible from the stress–displacement curves in Fig. 4b, only a minor influence of plastic deformation is assumed as the slope flattens marginally with increasing displacement.

The 50 × turned specimens exhibit increased J–integral values compared to the 5 × turned specimens. Hence, mean values of 9. 7 ± 1.1 MPa$\sqrt{m}$ for K_J and 402 ± 89 J/m^2 for the maximal J–integral

were evaluated from micromechanical fracture experiments [35]. As evidenced in the stress–displacement curves in Fig. 4c, a distinct plastic share during the experiments is evident. Here, the displacement of the indenter tip until the fatal crack event was 75% larger compared to the one of the 5 × turned specimens regardless of similar specimen geometries. However, a drop in stress after reaching maximum values occurs in advance of the final crack event. Despite the higher deformed state of this specimen condition, higher capable deformation prior to crack propagation and final failure was determined. This may originate in the stronger mechanical intermixing of Cu in W grains and vice versa [21,22,40].

Based on SEM investigations, no μm–sized W grains within the *nc* W–Cu composite of the 50 × turned specimens could be determined. Also, post–mortem analysis of the fractured surfaces evidenced no remaining coarse W grains along the crack path. This may explain the enhanced *J*–integral, but lower stress values at failure of the 50 × turned specimen condition. Hence, the *nc* W-Cu composite enables higher plasticity compared to the composite including several remaining coarse W grains. During crack propagation, these W grains act as internal flaws and fail due to their low K_{IC} values along the preferred {100} cleavage planes at RT [53-55]. As these planes are oriented randomly within the hosting *nc* W-Cu matrix, the crack deviates frequently from its path and a ragged fracture surface is created.

Typically, a higher amount of cracked surface would also evoke higher *J*–integral values. However, the negative effect of brittle cleavage of coarse W grains exceeds the crack deflecting properties [56,57]. Based on the microstructural investigation, the microstructure of the 50 × turned specimens is assumed to have reached a state of saturation in regards of the present grain size. Apart from the fact that dislocation motion is hampered in the *nc* W and Cu grains, dislocation formation and diffusion assisted motion along the multitude of grain boundaries allows earlier and easier yielding [58,59]. Hence, lower maximum stresses are reached as compared to the 5 × turned specimens (see Fig. 4b and c). However, this allows higher deformation and supports improved *J*–integral values in the case of the higher deformed specimens [58]. This is substantiated by the low *J*–integral value, measured during the cleavage of a single W grain in the case of specimen 0.5×_c1. Therefore, decreased *J*–integral, but higher fracture stresses at the failure of the 5 × turned specimen are evident.

The minor uncertainty of 13.2% (38 J/m^2) in the case of the 5 × deformed specimen indicates a rather homogenous distribution of remaining W grains within the *nc* W-Cu matrix. Regarding the fractured surfaces of 5 × and 50 × turned specimens, shown in Fig. 5d and e, respectively, distinct differences can be determined. Several small cleaved W grains are visible in the SE SEM images in the case of 5 × deformed specimens. Representatively, Fig. 5d displays the fractured surfaces of specimen 5×_c2, including transcrystalline fractured W grains, whereby two of them are highlighted by white arrows. Along the fractured surface of the 50 × turned specimen 50×_c3, no single cleaved coarse W grains, but a plane appearance is evident. The remaining roughness can be attributed to the grain size of this specimen condition.

Another effect may originate in the amount of mechanical alloyed W within Cu and vice versa [21,22,40]. Using atom probe tomography experiments, Kormout *et al.* [22] determined ∼ 4 at.% of Cu within W and 5 at.% W within the Cu phase regarding the same alloy composition. Despite the different crystal structures, intermixing is possible, as the applied pressure during HPT forces the atoms into their respective other phases. During TEM investigations, precipitates within the *nc* W grains could be determined (see white arrows in Fig. 2a and b. As a certain solubility of Cu

and W is prevalent within the mutual phases due to mechanical alloying during the HPT process, precipitation of sub nm–sized Cu or W particles is possible during annealing or retaining to ambient conditions [21]. Furthermore, mechanical alloying is suggested by XRD, as the Cu phase fraction decreased with an increasing deformation ratio. Hence, the formation of numerous dislocations along the different interfaces may assist the yielding process and hampers crack propagation in the heavily deformed 50 × specimens. However, precipitations of sub nm–sized particles within the W grains were equally distributed within both specimen conditions.

5. Conclusions

In this study, a coarse-grained W-Cu rod material was deformed via a high-pressure torsion process route. Different amounts of deformation resulted in unique microstructures and finally, a nano-crystalline W-Cu composite was obtained upon applying 50 turns at room temperature. Furthermore, a strong dependence of the determined *J*–integral on these microstructures during the in–situ experiments was observed. In the case of the 0.5 × turned specimen, site-specific microstructures led to different mechanical responses. The remaining but elongated W grains persisted in the μm regime, while in between these coarse W grains, a pancake–like structure was formed. Here, the high deformability of Cu in combination with the strength of W grains resulted in the highest measured *J*-integral. This is evident, as the intermediate Cu grains were deformed and distinct blunting was determined by secondary electron microscopy videos captured during in–situ experiments. When the notch was situated within a coarse W grain, the lowest *J*–integral and moderate failure stresses were measured. Here, the fractured surface exhibits a smooth appearance as the W grain was cleaved and no blunting of the crack tip was visible during the in-situ experiment.

Furthermore, the 5 × and 50 × deformed specimens exhibit a more brittle fracture behaviour as the mean grain sizes of their nanocrystalline matrix were decreased to 6.7 ± 3.2 and 7.0 ± 3.1 nm, respectively. Hence, an effective Hall–Petch hardening effect and therefore increased failure stresses could be achieved for both conditions. This is further substantiated by the determined hardness from nanoindentation tests, ranging from 8.0 ± 0.6 GPa for the 5 × deformed to 8.4 ± 0.7 GPa for the 50 × deformed specimens. The 50 × turned specimen exhibits no remaining coarse W grains within the *nc* WCu microstructure compared to the 5 × turned condition. Therefore, higher deformation prior to the fatal crack event was possible in the case of the 50 × turned specimen. This also leads to higher mean *J*-integral, but lower failure stresses compared to the 5 × turned specimen.

Based on these results, the influence of the high-pressure torsion process on the microstructure of a W-Cu composite and the resulting micromechanical fracture properties could be described. This enables to determine an optimal degree of deformation to enable a tailored nanocrystalline microstructure in combination with the highest mechanical properties.

CRediT authorship contribution statement

Michael Burtscher: Conceptualization, Methodology, Software, Investigation, Visualization, Validation, Writing – original draft. **Markus Alfreider:** Methodology, Investigation, Validation, Writing – review & editing. **Christina Kainz:** Investigation, Writing – review & editing. **Klemens Schmuck:** Software, Formal analysis, Writing – review & editing. **Daniel Kiener:** Supervision, Conceptualization, Funding acquisition, Writing – review & editing.

Data Availability

The raw/processed data required to reproduce these findings cannot be shared at this time as the data also forms part of an ongoing study.

Declaration of Competing Interest

The authors declare that they have no known competing financial interests or personal relationships that could have appeared to influence the work reported in this paper.

Acknowledgement

Appendix A. Supplementary data

Supplementary data to this article can be found online at https://doi.org/10.1016/j.matdes.2022.110848.

References

[1] P.G. Slade, Advances in material development for high power, vacuum interrupter contacts, IEEE Trans. Comp., Packag., Manufact. Technol. A 17 (1) (1994) 96–106, https://doi.org/10.1109/95.296374.

[2] H. Xie, W. Guan, H. Lv, H. Yang, M. Gao, Y. Fang, J. Liu, H. Wang, W-Cu/Cu composite electrodes fabricated via laser surface alloying, Materials Characterization 185 (2022) 111715, https://doi.org/10.1016/j.matchar.2021.111715.

[3] A.v. Müller, B. Böswirth, V. Cerri, H. Greuner, R. Neu, U. Siefken, E. Visca, J.H. You, Application of tungsten–copper composite heat sink materials to plasma-facing component mock-ups, Phys. Scr. T171 (2020) 014015, https://doi.org/10.1088/1402-4896/ab4142.

[4] E. Tejado, A. Müller, J.-H. You, J.Y. Pastor, The thermo-mechanical behaviour of W-Cu metal matrix composites for fusion heat sink applications: The influence of the Cu content, J. Nuclear Materials 498 (2018) 468–475, https://doi.org/10.1016/j.jnucmat.2017.08.020.

[5] S. Pietranico, S. Pommier, S. Lefebvre, S. Pattofatto, Thermal fatigue and failure of electronic power device substrates, Int. J. Fatigue 31 (11–12) (2009) 1911–1920, https://doi.org/10.1016/j.ijfatigue.2009.03.011.

[6] M. Arita, A. Takahashi, Y. Ohno, A. Nakane, A. Tsurumaki-Fukuchi, Y. Takahashi, Switching operation and degradation of resistive random access memory composed of tungsten oxide and copper investigated using in-situ TEM, Sci Rep 5 (2015) 17103, https://doi.org/10.1038/srep17103.

[7] A. Khalajhedayati, Z. Pan, T.J. Rupert, Manipulating the interfacial structure of nanomaterials to achieve a unique combination of strength and ductility, Nat. Commun. 7 (2016) 10802, https://doi.org/10.1038/ncomms10802.

[8] M. Wurmshuber, S. Doppermann, S. Wurster, D. Kiener, Ultrafine-grained Tungsten by High-Pressure Torsion – Bulk precursor versus powder processing route, IOP Conf. Ser.: Mater. Sci. Eng. 580 (1) (2019) 012051, https://doi.org/10.1088/1757-899X/580/1/012051.

[9] R.W. Armstrong, 60 Years of Hall-Petch: Past to Present Nano-Scale Connections, Materials Transactions 55 (1) (2014) 2–12.

[10] R.Z. Valiev, I.V. Alexandrov, Y.T. Zhu, T.C. Lowe, Paradox of Strength and Ductility in Metals Processed Bysevere Plastic Deformation, J. Mater. Res. 17 (1) (2002) 5–8, https://doi.org/10.1557/JMR.2002.0002.

[11] H.W. Höppel, J. May, P. Eisenlohr, M. Göken, Strain-rate sensitivity of ultrafine-grained materials, MEKU 96 (6) (2005) 566–571.

[12] A. Hohenwarter, R. Pippan, Fracture and fracture toughness of nanopolycrystalline metals produced by severe plastic deformation, Philos. Trans. A Math. Phys. Eng. Sci. 373 (2038) (2015), https://doi.org/10.1098/rsta.2014.0366.

[13] R. Pippan, A. Hohenwarter, The importance of fracture toughness in ultrafine and nanocrystalline bulk materials, Mater. Res. Lett. 4 (3) (2016) 127–136, https://doi.org/10.1080/21663831.2016.1166403.

[14] V. Richter, M. Ruthendorf, On hardness and toughness of ultrafine and nanocrystalline hard materials, Int. J. Refractory Metals Hard Materials 17 (1–3) (1999) 141–152, https://doi.org/10.1016/S0263-4368(99)00003-7.

[15] M. Roedig, W. Kuehnlein, J. Linke, M. Merola, E. Rigal, B. Schedler, E. Visca, Investigation of tungsten alloys as plasma facing materials for the ITER divertor, Fusion Eng. Design 61-62 (2002) 135–140, https://doi.org/10.1016/S0920-3796(02)00113-8.

[16] A. Muller, D. Ewert, A. Galatanu, M. Milwich, R. Neu, J.Y. Pastor, U. Siefken, E. Tejado, J.H. You, Melt infiltrated tungsten–copper composites as advanced heat sink materials for plasma facing components of future nuclear fusion devices, Fusion Engineering Design 124 (2017) 455–459, https://doi.org/10.1016/j.fusengdes.2017.01.042.

[17] J.W. Davis, K.T. Slattery, D.E. Driemeyer, M.A. Ulrickson, Use of tungsten coating on iter plasma facing components, J. Nuclear Materials 233–237 (1996) 604–608, https://doi.org/10.1016/S0022-3115(96)00209-7.

[18] M. Zhao, I. Issa, M.J. Pfeifenberger, M. Wurmshuber, D. Kiener, Tailoring ultra-strong nanocrystalline tungsten nanofoams by reverse phase dissolution, Acta Materialia 182 (2020) 215–225, https://doi.org/10.1016/j.actamat.2019.10.030.

[19] R. Juárez, J.P. Catalan, F. Ogando, A.J. Lopez-Revelles, P. Sauvan, S. Jakhar, E. Polunovskiy, M. Loughlin, J. Sanz, ITER plasma source and building modelling to produce radiation maps, Nucl. Fusion 58 (12) (2018) 126012, https://doi.org/10.1088/1741-4326/aadf9c.

[20] C. Hou, X. Song, F. Tang, Y. Li, L. Cao, J. Wang, Z. Nie, W-Cu composites with submicron- and nanostructures: progress and challenges, NPG Asia Mater 11 (1) (2019), https://doi.org/10.1038/s41427-019-0179-x.

[21] D. Edwards, I. Sabirov, W. Sigle, R. Pippan, Microstructure and thermostability of a W-Cu nanocomposite produced via high-pressure torsion, Philosophical Magazine 92 (33) (2012) 4151–4166, https://doi.org/10.1080/14786435.2012.704426.

[22] K.S. Kormout, R. Pippan, A. Bachmaier, Deformation-Induced Supersaturation in Immiscible Material Systems during High-Pressure Torsion, Adv. Eng. Mater. 19 (4) (2017) 1600675, https://doi.org/10.1002/adem.201600675.

[23] T. Hebesberger, H.P. Stüwe, A. Vorhauer, F. Wetscher, R. Pippan, Structure of Cu deformed by high pressure torsion, Acta Materialia 53 (2) (2005) 393–402, https://doi.org/10.1016/j.actamat.2004.09.043.

[24] I. Sabirov, O. Kolednik, R.Z. Valiev, R. Pippan, Equal channel angular pressing of metal matrix composites: Effect on particle distribution and fracture toughness, Acta Materialia 53 (18) (2005) 4919–4930, https://doi.org/10.1016/j.actamat.2005.07.010.

[25] W.C. Oliver, G.M. Pharr, An improved technique for determining hardness and elastic modulus using load and displacement sensing indentation experiments, J. Mater. Res. 7 (6) (1992) 1564–1583, https://doi.org/10.1557/JMR.1992.1564.

[26] C.P. Liang, C.Y. Wu, J.L. Fan, H.R. Gong, Structural, thermodynamic, and mechanical properties of WCu solid solutions, J. Physics Chemistry Solids 110 (2017) 401–408, https://doi.org/10.1016/j.jpcs.2017.06.034.

[27] R.A. Young, The Rietveld method, Oxford Univ. Press, Oxford, 2002.

[28] M.J. Pfeifenberger, V. Nikolić, S. Žák, A. Hohenwarter, R. Pippan, Evaluation of the intergranular crack growth resistance of ultrafine grained tungsten materials, Acta Materialia 176 (2019) 330–340, https://doi.org/10.1016/j.actamat.2019.06.051.

[29] M. Alfreider, D. Kozic, O. Kolednik, D. Kiener, In-situ elastic-plastic fracture mechanics on the microscale by means of continuous dynamical testing, Materials & Design 148 (2018) 177–187, https://doi.org/10.1016/j.matdes.2018.03.051.

[30] M. Alfreider, S. Kolitsch, S. Wurster, D. Kiener, An analytical solution for the correct determination of crack lengths via cantilever stiffness, Materials & Design 194 (2020) 108914, https://doi.org/10.1016/j.matdes.2020.108914.

[31] S. Wurster, C. Motz, R. Pippan, Characterization of the fracture toughness of micro-sized tungsten single crystal notched specimens, Philosophical Magazine 92 (14) (2012) 1803–1825, https://doi.org/10.1080/14786435.2012.658449.

[32] R. Margevicius, J. Riedle, P. Gumbsch, Fracture toughness of polycrystalline tungsten under mode I and mixed mode I/II loading, Materials Sci. Engineering: A 270 (2) (1999) 197–209, https://doi.org/10.1016/S0921-5093(99)00252-X.

[33] D. Rahmatabadi, B. Mohammadi, R. Hashemi, T. Shojaee, An Experimental Study of Fracture Toughness for Nano/Ultrafine Grained Al5052/Cu Multilayered Composite Processed by Accumulative Roll Bonding, J. Manufacturing Sci. Engineering 140 (10) (2018), https://doi.org/10.1115/1.4040542.

[34] A. Singh, L. Tang, M. Dao, L. Lu, S. Suresh, Fracture toughness and fatigue crack growth characteristics of nanotwinned copper, Acta Materialia 59 (6) (2011) 2437–2446, https://doi.org/10.1016/j.actamat.2010.12.043.

[35] ASTM Standard E1820-20. Test Method for Measurement of Fracture Toughness. West Conshohocken, PA: ASTM International; 2020. 10.1520/E1820-20.

[36] ASTM Standard E399-09. Test Method for Linear-Elastic Plane-Strain Fracture Toughness KIc of Metallic Materials. West Conshohocken, PA: ASTM International; 2009. 10.1520/E0399-09.

[37] I. Sabirov, R. Pippan, Formation of a W-25%Cu nanocomposite during high pressure torsion, Scripta Materialia 52 (12) (2005) 1293–1298, https://doi.org/10.1016/j.scriptamat.2005.02.017.

[38] D.E. Armstrong, A.J. Wilkinson, S.G. Roberts, Measuring anisotropy in Young's modulus of copper using microcantilever testing, J. Mater. Res. 24 (11) (2009) 3268–3276, https://doi.org/10.1557/jmr.2009.0396.

[39] H.M. Rietveld, A profile refinement method for nuclear and magnetic structures, J. Appl. Crystallogr. 2 (2) (1969) 65–71, https://doi.org/10.1107/S0021889869006558.

[40] T. Aboud, B.-Z. Weiss, R. Chaim, Mechanical alloying of the immiscible system W-Cu, Nanostructured Materials 6 (1–4) (1995) 405–408, https://doi.org/10.1016/0965-9773(95)00082-8.

[41] J.-C. Kim, I.-H. Moon, Sintering of nanostructured W-Cu alloys prepared by mechanical alloying, Nanostructured Materials 10 (2) (1998) 283–290, https://doi.org/10.1016/S0965-9773(98)00065-8.

[42] M. Burtscher, M. Zhao, J. Kappacher, A. Leitner, M. Wurmshuber, M. Pfeifenberger, V. Maier-Kiener, D. Kiener, High-Temperature Nanoindentation of an Advanced Nano-Crystalline W/Cu Composite, Nanomaterials (Basel) 11 (11) (2021) 2951, https://doi.org/10.3390/nano11112951.

[43] H.S. Kim, S.I. Hong, S.J. Kim, On the rule of mixtures for predicting the mechanical properties of composites with homogeneously distributed soft and hard particles, J. Materials Processing Technology 112 (1) (2001) 109–113.

[44] Y.A. Chang, L. Himmel, Temperature Dependence of the Elastic Constants of Cu, Ag, and Au above Room Temperature, J. Applied Physics 37 (9) (1966) 3567–3572, https://doi.org/10.1063/1.1708903.

[45] R. Lowrie, A.M. Gonas, Dynamic Elastic Properties of Polycrystalline Tungsten, 24°–1800°C, J. Applied Physics 36 (7) (1965) 2189–2192, https://doi.org/10.1063/1.1714447.

[46] G. Wilde, H. Rösner, Stability aspects of bulk nanostructured metals and composites, J. Mater. Sci. 42 (5) (2007) 1772–1781, https://doi.org/10.1007/s10853-006-0986-7.

[47] F. Tang, D.S. Gianola, M.P. Moody, K.J. Hemker, J.M. Cairney, Observations of grain boundary impurities in nanocrystalline Al and their influence on microstructural stability and mechanical behaviour, Acta Materialia 60 (3) (2012) 1038–1047, https://doi.org/10.1016/j.actamat.2011.10.061.

[48] G.A. Langer, G. Erdélyi, Z. Erdélyi, G. Csiszár, Determination of diffusion coefficients in immiscible systems: Cu W as an example, Materialia 6 (2019), https://doi.org/10.1016/j.mtla.2019.100342 100342.

[49] J. Ast, M. Göken, K. Durst, Size-dependent fracture toughness of tungsten, Acta Materialia 138 (2017) 198–211, https://doi.org/10.1016/j.actamat.2017.07.030.

[50] M.A. Monclús, M. Karlik, M. Callisti, E. Frutos, J. LLorca, T. Polcar, J.M. Molina-Aldareguía, Microstructure and mechanical properties of physical vapor deposited Cu/W nanoscale multilayers: Influence of layer thickness and temperature, Thin Solid Films 571 (2014) 275–282, https://doi.org/10.1016/j.tsf.2014.05.044.

[51] J.M. Wheeler, R. Raghavan, V. Chawla, J. Zechner, I. Utke, J. Michler, Failure mechanisms in metal–metal nanolaminates at elevated temperatures: Microcompression of Cu–W multilayers, Scripta Materialia 98 (2015) 28–31, https://doi.org/10.1016/j.scriptamat.2014.11.007.

[52] T. Sumigawa, T. Shishido, T. Murakami, T. Iwasaki, T. Kitamura, Evaluation on plastic deformation property of copper nano-film by nano-scale cantilever specimen, Thin Solid Films 518 (21) (2010) 6040–6047, https://doi.org/10.1016/j.tsf.2010.06.039.

[53] J. Riedle, P. Gumbsch, H.F. Fischmeister, Cleavage anisotropy in tungsten single crystals, Phys Rev Lett 76 (19) (1996) 3594–3597, https://doi.org/10.1103/PhysRevLett.76.3594.

[54] D. Hull, P. Beardmore, A.P. Valintine, Crack propagation in single crystals of tungsten, Philosophical Magazine: A J. Theoretical Experimental Applied Physics 12 (119) (1965) 1021–1041, https://doi.org/10.1080/14786436508228132.

[55] M. Faleschini, H. Kreuzer, D. Kiener, R. Pippan, Fracture toughness investigations of tungsten alloys and SPD tungsten alloys, J. Nuclear Materials 367–370 (2007) 800–805, https://doi.org/10.1016/j.jnucmat.2007.03.079.

[56] S. Gabel, S. Giese, B. Merle, I. Sprenger, M. Heilmaier, S. Neumeier, E. Bitzek, M. Göken, Microcantilever Fracture Tests on Eutectic NiAl–Cr(Mo) In Situ Composites, Adv. Eng. Mater. 23 (6) (2021) 2001464, https://doi.org/10.1002/adem.202001464.

[57] R. Pippan, S. Wurster, D. Kiener, Fracture mechanics of micro samples: Fundamental considerations, Materials & Design 159 (2018) 252–267, https://doi.org/10.1016/j.matdes.2018.09.004.

[58] J. Schiøtz, F.D. Di Tolla, K.W. Jacobsen, Softening of nanocrystalline metals at very small grain sizes, Nature 391 (6667) (1998) 561–563.

[59] A. Giga, Y. Kimoto, Y. Takigawa, K. Higashi, Demonstration of an inverse Hall-Petch relationship in electrodeposited nanocrystalline Ni–W alloys through tensile testing, Scripta Materialia 55 (2) (2006) 143–146, https://doi.org/10.1016/j.scriptamat.2006.03.047.